THE NUMERICAL MODELLING APPROACH FOR THE SIMULATION OF RIVER MEANDERING PROCESS IN WAINGANGA RIVER

Dr. N.L. Dongre, IPS, Ph.D., DLitt**

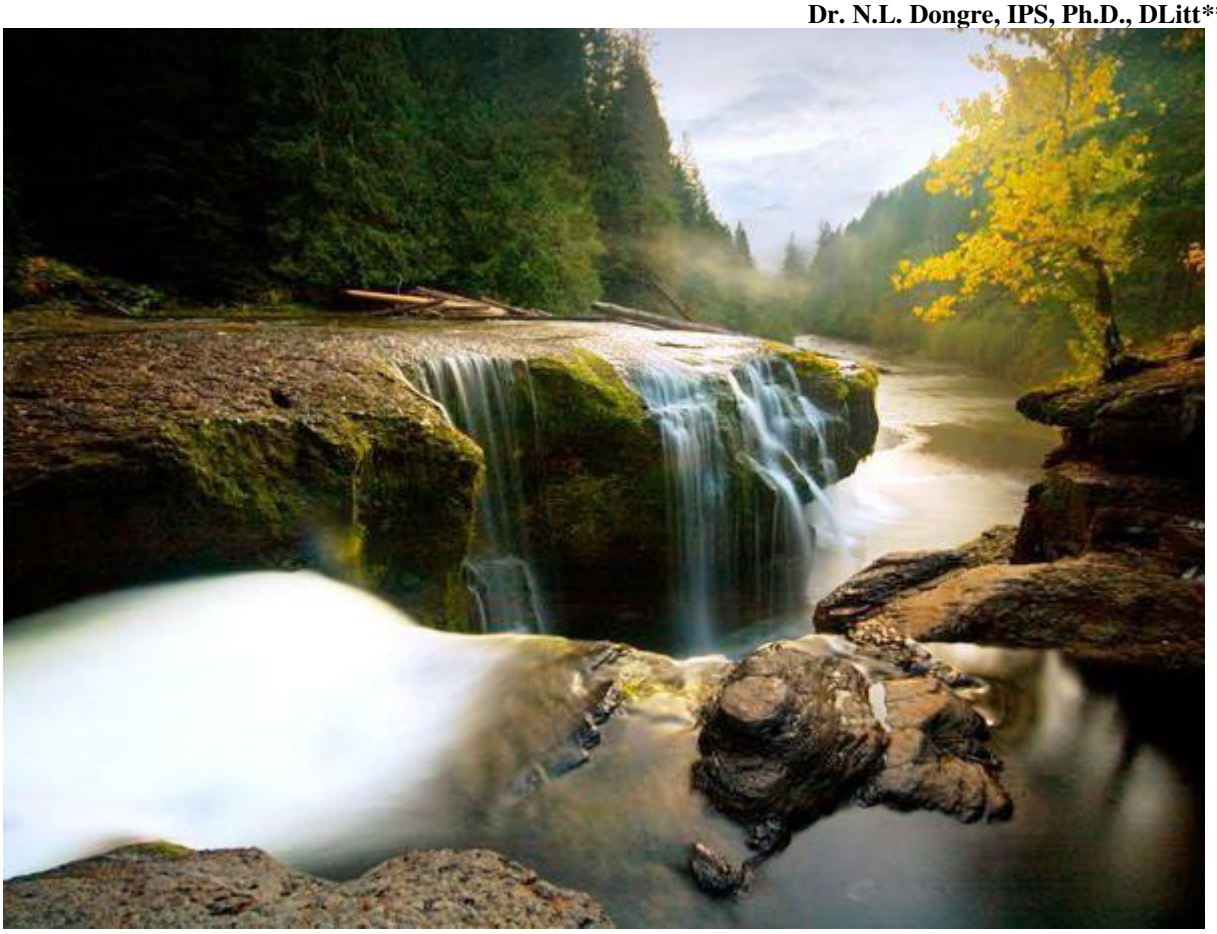

The flow momentam and re-distribution of bed rocks degenerated near concave bank passes retreat as bank erosion occurred the eye catching waterfall on the upper Son river, tributary of Wainganga.

Abstract

The channel meandering inception is the outcome of the complex interaction between flow, bed sediment, and bank material. A model of depth-averaged two-dimensional hydrodynamic is developed to simulate the inception and channel meandering development processes. The sediment transport model calculates both bedload and suspended load expecting equilibrium sediment transport. Bank erosion consists of two interactive processes: basal erosion and bank failure. Basal erosion is calculated from a newly derived equation for the entrain-ment of sediment particles by hydrodynamic forces. The mass conservation equation, where basal erosion and bank failure are considered source terms, was solved to obtain the rate of bank erosion. The parallel bank failure model was tested with the laboratory experiments of Friedkin on the initiation and evolution processes of non-cohesive meandering channels.

****Dr. N.L. Dongre**
C-14 Jaypee Nagar Rewa 486450
Email: - nl.dongre@jalindia.co.in dongrenl@gmail.com
Mobile No. 7869918077, 09425152076

The model replicates the downstream translation and lateral extension of meandering loops reasonably well. Plots of meandering planforms illustrate the evolution of sand bars and redistribution of flow momentum in meandering channels. This numerical modelling study demonstrates the potential of depth-integrated two-dimensional models for the simulation of meandering processes. The model correctly replicates the different phases of the evolution of free meandering channels in experimental laboratory settings including: (1) downstream and upstream migration; (2) lateral extension; and (3) rotation of meander bends.

Keywords: meandering channel; sediment transport; numerical model; bank erosion

Introduction

The meandering channels' lateral migration, denoting the complex mechanism of fluid dynamics, sediment transport and bank erosion, has intrigued geomorphologists for many years. Begining from straight channels, alternate bars and pools form which further extends the initiation of meandering. Flow converges to the concave banks and diverges at the convex banks due to the centrifugal force that generates a spiral flow in meandering channels. Flow momentum redistribution causes bed degradation near concave banks and deposition near convex banks. Bed degradation steepens concave banks whereas deposition stabilizes convex banks. This causes concave banks to retreat as bank erosion occurs, while convex banks advance with the build-up of point bars. Therefore, the migration of meandering channels is accompanied with an increase in meandering amplitude and wavelength, downstream translation, lateral extension, rotation, and formation of chute cutoffs.

The formation model or evolution of meanders, both process-based (Ikeda *et al.,* 1981; Ikeda and Nishimura, 1986) and physically based (Osman and Thorne, 1988) bank erosion models are attainable. Process-based models assume a rate of bank erosion proportional to near-bank flow velocity. In contrast, physically based models calculate sediment transport and bank erosion rates to determine the advance and retreat of channel bankline. However, the erosion coefficient in process-based models is empirical and does not reflect bank geometry and bank material at specific locations in natural meanders. Process-based models can be effective in predicting the long-term behaviour of meandering rivers (Parker and Andrews, 1986; Sun *et al.,* 1996; Lancaster and Bras, 2002). Physically based models can be specifically used to determine the rate of bank erosion at individual locations within a natural meandering channel by knowing the flow field, bank geometry and bank material. They are expected to become more successful in predicting immediate or short-term geomorphic responses to river modifications.

With the fast development of mathematical models and advances in computer technology, two- and three-dimensional computational fluid dynamic (CFD) models have become increasingly famous to simulate morphodynamic processes of natural rivers, meandering streams (Mosselman, 1998; Duan *et al,* 2001; Olsen, 2003), and braiding channels (Nicholas and Smith, 1999). This paper adds a bank erosion model to a two-dimensional, depth-averaged model and applied it to the Wainganga River, a meandering gravel-bed river between Dhuti ghat and confluence of Waingnanga with Bagh River in Madhya Pradesh State, India. Poor agreement between modelling results and observations were ascribed to the shortcomings of the flow model rather than to the bank erosion subroutines. Duan *et al.* (2001) solved the two-dimensional, depth-averaged momentum and continuity equations expressed in Cartesian coordinates for the flow field. The secondary flow-correction term (Engelund, 1974) was then implemented to redirect the transport of bedload sediment from the calculated depth-averaged velocity. A new bank erosion model derived from the mass conservation law for near-bank cells was employed to simulate the migration of bank lines. The simulated initiation, migration and evolution of a meander indicated that the rate of bank erosion is a function of longitudinal gradient in sediment transport, strength of secondary flow, and mass wasting from bank erosion. Although sediment transport and basal bank erosion were considered, the geotechnical bank failure of cohesive bank material following basal erosion was neglected (Duan *et al.,* 2001). As a result, the simulated meandering wavelength and amplitude did not agree with the observations described in Friedkin (1945).

Darby *et al.* (2002) substituted the bank erosion subroutine within the two-dimensional, depth-averaged numerical model RIPA with a new physically based bank erosion model. Within this algorithm,

basal erosion of cohesive bank material and subsequent bank failure as well as transport and deposition of eroded bank material were simulated to predict the evolution of meandering channels. The rate of basal erosion of cohesive material was obtained by applying a simple model (ASCE Task Committee, 1998) where the rate of basal erosion is an exponential function of the excessive shear stress. The mass volume of bank failure was calculated from the bank erosion model for cohesive bank material (Osman and Thorne, 1988). Then, the eroded bank material was divided into three groups according to grain size, and transported or deposited at bank toes as bedload or suspended load. The variation of coarse and fine sediments in sand bars was simulated with sediment transport calculations by size fractions. When the effects of secondary current on sediment transport were considered theoretically or empirically, the two-dimensional, depth-averaged hydrodynamic model combined with the sediment transport and bank erosion models became capable of modelling the evolutionary processes of meandering channels.

A full three-dimensional (3D) CFD model having the solutions of flow velocity in three dimensions has been applied successfully to simulate the formation of meandering streams in the laboratory (Olsen, 2003). A 3D CFD model can provide a flow field that is three-dimensional so that the secondary flow correction is not needed. Advances in the numerical scheme and computer resources potentially will reduce significantly the computational time. Olsen (2003) also stated that another advantage in using the 3D CFD model lies in its capability to simulate the morphodynamic process without a separate bank erosion model because a bank erosion model is not required when the entire basin is chosen as the computational domain.

This study submits a two-dimensional numerical model of Wainganga River (Balaghat district), Madhya Pradesh, India that connects a physically based bank erosion model with the bend migration model to simulate the formation process of meandering channels. The developed model encompasses: a depth-averaged, two-dimensional flow hydrodynamic model; a sediment transport model; and a bank erosion model. The flow hydrodynamic model simulating flow and mass dispersion in meandering channels is described in more details in Duan (2004). New components specific to this study include: (1) the direction of bedload transport is determined by combining the effects of secondary flow and transverse bed slope; and (2) the bank line retreat and advance can be calculated from near-bank mass conservation where bank material from basal erosion and bank failure are treated as source terms. This paper emphasizes the development and application of the sediment transport and bank erosion models. The goal of this simulation is to illustrate the modelling approach with potential applications to natural streams.

Flow Simulation

The governing equations for flow simulation are the depth-averaged Reynolds approximation of momentum equations (Equations 1 and 2) and continuity equation (Equation 3).

$$\frac{\partial(h\bar{u})}{\partial t}+\frac{\partial}{\partial x}(h\bar{u}^2)+\frac{\partial D_{uu}}{\partial x}+\frac{\partial}{\partial y}(h\bar{u}\bar{v})+\frac{\partial D_{uv}}{\partial y}=-\mathrm{g}h\frac{\partial \zeta}{\partial x}+\frac{\partial}{\partial x}(h\tau_{xx})+\frac{\partial}{\partial y}\left(h\tau_{xy}\right)-\tau_{bx} \quad (1)$$

$$\frac{\partial(h\bar{v})}{\partial t}+\frac{\partial}{\partial x}(h\bar{u}\bar{v})+\frac{\partial D_{uv}}{\partial x}+\frac{\partial}{\partial y}(h\bar{v}^2)+\frac{\partial D_{vv}}{\partial y}=-\mathrm{g}h\frac{\partial \zeta}{\partial y}+\frac{\partial}{\partial x}\left(h\tau_{yx}\right)+\frac{\partial}{\partial y}\left(h\tau_{yy}\right)-\tau_{by} \quad (2)$$

$$\frac{\partial h}{\partial t}+\frac{\partial}{\partial x}(h\bar{u})+\frac{\partial}{\partial y}(h\bar{v})=0 \quad (3)$$

where $\bar{u}$ and $\bar{v}$ are depth-averaged velocity components in x and y directions, respectively; t is time; ζ is surface elevation; h is flow depth; g is acceleration due to gravity; τ_{bx} and τ_{by} are friction shear stress terms at the bottom in x and y directions, respectively, written as

$$\tau_{bx}=\frac{n^2\mathrm{g}}{h^{\frac{1}{3}}}\bar{u}U \text{ and } \tau_{by}=\frac{n^2\mathrm{g}}{h^{\frac{1}{3}}}\bar{v}U$$

in which U is depth-averaged total velocity and n is Manning's roughness coefficient;τ_{xy}, τ_{xx}, τ_{yx}, and τ_{yy}, are Reynolds stress terms, that expressed as-

$$\tau_{xx} = 2v_t \frac{\partial \bar{u}}{\partial x}, \tau_{yy} = 2v_t \frac{\partial \bar{v}}{\partial y}, \quad \tau_{xy} = \tau_{yx} = v_t \left(\frac{\partial \bar{u}}{\partial y} + \frac{\partial \bar{v}}{\partial x} \right)$$

in which v_t is eddy viscosity; and $D_{uu'}$ D_{uv} and D_{vv} are dispersion terms resulting from the discrepancy between the depth-averaged velocity and the actual velocity, expressed as

$$D_{uu} = \int_{Z_0}^{Z_{0+h}} (u - \bar{u})^2 dz, D_{uv} = \int_{Z_0}^{Z_{0+h}} (u - \bar{u})(u - \bar{v})\, dz,\ D_{vv} = \int_{Z_0}^{Z_{0+h}} (v - \bar{v})^2 dz \quad (4)$$

where z_0 is zero velocity level.

The depth-averaged parabolic eddy viscosity model is adopted, where the depth-averaged eddy viscosity is obtained as

$$v_t = \frac{1}{6} k u_* h \quad (5)$$

where u_* is shear velocity and *k* is von Karman's constant.

To include the effect of secondary flow, four dispersion terms were added to the momentum equations. To derive the mathematical expressions of these terms, it is assumed that the streamwise velocity satisfies the logarithmic law, and then the streamwise velocity profile can be written as

$$\frac{u_l}{\bar{u}_l} = \frac{1\mathrm{n}\left(\frac{z}{z_0}\right)}{\frac{z_0}{h} - 1 + 1\mathrm{n}\left(\frac{h}{z_0}\right)} \quad (6)$$

where *z* is vertical coordinate; u_l and $\bar{u}_l$ are the streamwise and depth-averaged velocity, respectively; and u_* is shear velocity, and z_0 was calculated according to flow hydraulic smooth, transition and rough regimes.

The transverse velocity profile of the secondary flow is presumed to be linear. The profile of the transverse velocity proposed by Odgaard (1989a) was adopted in this model.

$$v_r = \bar{v}_r + 2v_s \left(\frac{z}{h} - \frac{1}{2} \right) \quad (7)$$

where $v_r, \bar{v}_r$ and v_s are the transverse velocity, the depth-averaged transverse velocity, and the transverse velocity at the water surface, respectively. Engelund (1974) derived the deviation angle of the bottom shear stress and gave that

$$\left(\frac{\tau_r}{\tau_l} \right)_b \approx \left(\frac{v_r}{u_l} \right)_b = 7.0 \frac{h}{r} \quad (8)$$

where r is the radius of channel curvature. According to Equation 7, the secondary flow velocities at the surface and the bottom are equal. As such, Equation 8 (Engelund, 1974) was taken as the transverse velocity at the surface. The dispersion terms at the streamwise and transverse directions can be expressed as

$$D_{uu}^c = \int_{Z_0}^{Z_{0+h}} (u_l - \bar{u}_l)^2 dz,\ D_{uv}^c = \int_{Z_0}^{Z_{0+h}} (u_l - \bar{u}_l)(v_r - \bar{v}_r)\, dz,\ D_{vv}^c = \int_{Z_0}^{Z_{0+h}} (v_r - \bar{v}_r)^2 dz, \quad (9)$$

where D_{uu}^c, D_{uv}^c, and D_{vv}^c denote dispersion terms in curvilinear coordinates. Substituting Equations 6, 7 and 8 into the above dispersion terms yields

$$D_{uu}^c = x^2 u_l^{-2} h[-\eta_0 1\mathrm{n}\, \eta_0 (1\mathrm{n}\, \eta_0 - 2) + 2\eta_0 (1 - \eta_0)(1 - 1\mathrm{n}\, \eta_0) - (\eta_0 - 1)^3] \quad (10)$$

$$D_{uv}^{c} = 49.0u_{l}^{-2}\frac{h^{3}}{r^{3}}\left[-\frac{1}{3}\eta_{0}^{3} + \frac{1}{2}\eta_{0}^{2} - \frac{1}{4}\eta_{0} + \frac{1}{12}\right] \quad (11)$$

$$D_{vv}^{c} = 3.5u_{l}^{-2}\frac{h^{2}}{r}[\eta_{0}^{2}\ 1\mathrm{n}\ \eta_{0} + \eta_{0}1\mathrm{n}\ \eta_{0} - \eta_{0} + \eta_{0}^{3}] \quad (12)$$

where $x = 1/(\ \eta_0 - 1 - 1\mathrm{n}\ \ \eta_0)$ and $\eta_0 = z_0/h$ is the dimensionless zero bed elevation. If θ_l denotes the angle between the streamwise direction and the positive *x*-axis, and θ_n is the angle between the transverse direction pointing to the outer bank and the positive *x*-axis, the depth-averaged velocities in curvilinear coordinates can be converted to those in Cartesian coordinates according to the following equations

$$\bar{u} = \bar{u}_l \cos\theta_l\ + \bar{v}_r \cos\theta_n \quad \bar{v} = \ \bar{u}_l \sin\theta_l\ + \bar{v}_r \sin\ \theta_n \quad (13)$$

Then, the dispersion terms in Cartesian coordinates can be correlated to those in curvilinear coordinates as follows

$$D_{uu} = \ D_{uu}^{c} \cos^2\theta_l\ + 2\ D_{uv}^{c} \cos\ \theta_l \cos\ \theta_n\ +\ D_{vv}^{c} \cos^2\theta_n \quad (14)$$

$$D_{vv} = \ D_{uu}^{c} \sin^2\theta_l\ + 2\ D_{uv}^{c} \sin\ \theta_l \sin\ \theta_n\ +\ D_{vv}^{c} \sin^2\theta_n \quad (15)$$

$$D_{uv} = \ D_{uu}^{c} \cos\theta_l\ \sin\theta_l\ +\ D_{uv}^{c}(\cos\ \theta_n \sin\theta_l\ + \sin\theta_n\ \cos\theta_l\ )+\ D_{vv}^{c} \sin\theta_n \mathrm{con}\ \theta_n \quad (16)$$

These dispersion terms were included in Equations 1 and 2 to solve for flow velocity. A more detailed description of the hydrodynamic model is given in Duan (2004).

Sediment Transport Simulation

Bedload transport

To presume bedload transport in a curved channel, at the most three forces should be considered. These forces consists bed shear stress due to longitudinal flow, bed shear stress due to curvature-induced secondary flow in the transverse direction, and component of gravitational force on the slope of the channel bed or bank. The influence of gravity on bedload transport is shown in its effect on incipient motion of sediment and direction of bedload transport.

Numerous equations are available to forcast the transport rate of bedload sediment. This study selected the Meyer-Peter and Muller bedload transport formula that is valid for uniform sediment with a mean particle size ranging from 0-23 to 28-6 mm. In this research, the bedload transport rate is computed by this formula as follows

$$q_b = C_m[(s-1)\mathrm{g}]^{0.5} d_{50}^{1.5}(\mu'\tau_* - \tau_{*c})^{1.5} \quad (17)$$

where q_b is the total bedload transport rate per unit width; $\tau_* = (\rho u_*^2)/[(\rho_s - \rho)\mathrm{g}d_{50}]$ is the effective particle mobility parameter; $\tau_{*c} = \tau_c/[(\rho_s - \rho)\mathrm{g}d_{50}]$ is the critical value of τ_* for incipient motion depending on particle Reynolds number $(R_e^* = (u_* d_{50})/v)$, and τ_{*c} = 0-047 when R_e^*> 100; constant coefficient C_m = 8-0; and the bed-form effect was ignored so that the factor $\mu'$was omitted in this model; d_{50} is the mean particle diameter;$s = \rho_s/\rho$, where ρ_s and ρ are densities of sand and water, respectively.

Bedload transport is deviated from the downstream flow direction because of the influence of the secondary flow and bed-transverse slope. The deviation angle is explained as the angle between the middle line of the channel and the direction of shear force at the bed. Engelund (1974), Kikkawa *et al.* (1976), Parker (1984), Bridge (1992) and Darby and Delbono (2002) derived relations to estimate the deviation angle based on the analytical solutions of flow field in sinuous channels. Among them, Bridge

(1992) and Darby and Delbono (2002) stressed that flow in the bend with a varying curvature is non-uniform, so steady and non-uniform flow momentum equations are necessary when solving the flow field. As a result, the tangent of the deviation angle (Darby and Delbono, 2002) is not only a function of the mean longitudinal and transverse velocity components, local radius of the curvature and friction, but also varies spatially in the sine-generated bends. This study adopted the angle of deviation, *(5,* derived by Ikeda (1989)

$$tan\beta = \frac{u_{bn}}{u_{bs}} - \frac{1+\alpha\mu}{\lambda_s \mu}\sqrt{\frac{\tau_{*c}\,\partial z_b}{\tau_* \partial n}} = -N_* \frac{h}{r} - \frac{1+\alpha\mu}{\lambda_s \mu}\sqrt{\frac{\tau_{*c}\,\partial z_b}{\tau_* \partial n}} \tag{18}$$

where u_{bn} and u_{bs} are the transverse and longitudinal velocities near the bed; α=0.85, $\mu = \tan\phi$ and $\lambda_s = 0.59$ are friction coefficients, in which ϕ is the angle of repose; r is the radius of curvature; N_* is a coefficient that equals 7-0 derived by Engelund (1974); and $\partial z_b / \partial n$ denotes the transverse slope. The first term on the right of Equation 18 accounts for the effect of secondary flow velocity at the bottom, and the second term quantifies the effect of the transverse slope. The components of bedload transport in *x* and *y* directions of Cartesian coordinates can be obtained as

$$\begin{cases} q_{bx} = q_b \cos(\theta_t - \beta) \\ q_{by} = qb \sin(\theta_t - \beta) \end{cases} \tag{19}$$

where q_{bx} and q_{by} are components of bedload transport rate in *x* and *y* directions, respectively; and θ_t is the angle between the centreline and positive *x* axis as defined in the flow model.

The gravity component impedes the motion of sediment particles resting on a sloping bed because gravity may or may not influence in the same direction as the fluid shear force. Van Rijn (1989) proposed a formula to account for this slope effect. In the case of a longitudinal sloping bed (in the bed-shear stress direction), the critical shear stress τ_{*c} is written as

$$\tau_{*c} = K_1 \tau_{*c,0} \tag{20}$$

where $\tau_{*c\,0,}$ is the critical mobility parameter on a horizontal bottom, which can be predicted from Shield's curve. The coefficient K_1 is defined as

$$K_1 = \mathrm{Sin}(\phi - \beta_1)/\sin\phi \text{ (for a downsloping bed)} \tag{21}$$

$$K_1 = \mathrm{Sin}(\phi - \beta_1)/\sin\phi \text{ (for a downsloping bed)} \tag{22}$$

where ϕ is the angle of repose; and β_1 is the longitudinal bed-slope angle. This formulation has been developed by Bormann and Julien (1990). In the case of a transverse sloping bed, the critical bed shear stress is

$$\tau_{*c} = K_2 \tau_{*c\,0,} \tag{23}$$

where $K_2[\cos\beta_2][1 - (\tan^2\beta_2/\tan\phi)]^{-0.5} = \beta_2$ ($_2$ is the transversal bed-slope angle. This formulation is attributed to Lane, as recently described in Julien (2002). For a combined longitudinal and transversal bed slope, the following relation is used

$$\tau_{*c} = K_1 K_2 \tau_{*c\,0,} \tag{24}$$

Suspended load transport

To estimate the rate of suspended sediment transport, a suspended sediment concentration profile must be presumed. In the present model, the classic Rouse profile (van Rijn, 1989) is presumed to be valid at $z = a$ from the channel bed to the water surface. The Rouse profile is written as

$$\frac{C}{C_a} = \left(\frac{h-z}{z}\frac{a}{h-a}\right)^z \tag{25}$$

where a is the reference bed level; z is the distance from the bottom; Z is the Rouse number; and C and C_a are concentrations of suspended sediment and its value at $z = a$, respectively. The expression of the Rouse number is given as

$$Z = \frac{\omega}{k\beta' u_*} \tag{26}$$

Where ω is the falling velocity; k = 0-4 is von Karman's constant; $u_*$is the shear velocity, and β describes (van Rijn, 1989) the difference in the diffusion of a sediment particle from the diffusion of a fluid 'particle'. The coefficientβ is calculated as

$$\beta' = 1 + 2\left(\frac{\omega}{u_*}\right)^2 ; 0.1 < \frac{\omega}{u_*} < 1 \tag{27}$$

The suspended sediment transport rate is the result of the velocity profile and the suspended sediment concentration profile. The longitudinal velocity profile satisfies the logarithmic law and is explained in Equation 6. The transverse velocity profile of the secondary flow was accepted to be linear and satisfied Equation 7. The right-hand side of Equation 7 has two terms: one is the depth-averaged secondary flow velocity relating to bed topography, and the other has a zero value if integrating over flow depth.

The van Rijn (1989) formula was adopted here for computing the reference concentration

$$C_a = 0.015 \frac{d_{50}}{a} \frac{T^{1.5}}{D_*^{0.3}} \tag{28}$$

Where

$$D_* = d_{50}\left[\frac{(s-1)g}{v^2}\right]^{\frac{1}{3}}$$

is the dimensionless particle diameter;

$$T = \frac{\tau_* - \tau_{*c}}{\tau_{*c}} \tag{29}$$

where τ_* is the dimensionless grain shear stress parameter, and τ_{*c} is the critical bed-shear stress according to Equation 24. Knowing the longitudinal and transverse velocity profiles (Equations 6 and 7) and the concentration of suspended sediment (Equation 25), the suspended sediment transport rates in the longitudinal and transverse directions can be obtained as

$$q_{sl} = \int_{z_0}^{h} u_l \, C dz; \; q_{sr} = \int_{z_0}^{h} v_r \, C dz \tag{30}$$

where q_{sl} and q_{sr} are the suspended sediment transport rates in the longitudinal and transverse directions, respectively. Because the Cartesian coordinates are used in this model, the longitudinal and transversal components of the suspended sediment transport rate were transformed into the x and y components of the Cartesian coordinates through the following equations

$$q_{sx} = q_{sl} \cos\theta_l + q_{sr} \cos\theta_r \tag{31}$$

$$q_{sy} = q_{sl} \sin\theta_l + q_{sr} \sin\theta_r \tag{32}$$

where θ_l and θ_r are the angles defined in Equation 13, and q_x and q_y are the total suspended loads in x and y directions, respectively.

Computation of bed-elevation change

The sediment continuity equation is then used for calculating bed-elevation changes

$$(1-\rho)\frac{\partial z_b}{\partial t}+\frac{\partial(q_{bx}+q_{sx})}{\partial x}+\frac{\partial(q_{by}+q_{sy})}{\partial y}=0 \tag{33}$$

where p is the porosity of the bed and bank material, and z_b is the bed elevation.

Bank Erosion Simulation

Erosion of Bank contains two physical processes: basal erosion and bank failure (Osman and Thorne, 1988; Darby and Thorne, 1996). Basal erosion refers to the fluvial entrainment of bank material by flow-induced forces that work on the bank surface: drag force, resistance force, and lift force. Bank failure happens due to geotechnical instability (e.g. planar failure, rotational failure, sapping or piping). Bank erosion does not permit the retreat of bank line because the eroded bank material may be deposited close to the banks. The rate of bank erosion is calculated empirically from the geometry of channel bends, bank material, and flow intensity (Hooke, 1995). Process-based bend migration models (Ikeda *et al.,* 1981; Johannesson, 1985; Odgaard, 1989a,b; Crosato, 1990; Sun *et al,* 2001a,b) were successfully applied for long-term trends in meandering evolution. Although the rate of bank erosion can be proportional to near-bank excess velocity, however, this assumption could be unrealistic if eroded bank material is deposited as sand bars.

The present model divides the calculation of bank erosion and the advance and retreat of bank lines. Sediment from basal erosion is calculated by using an analytical approach derived in Duan (2001). Mass wasting from bank failure is estimated using the parallel bank failure model for non-cohesive bank material. The contributions of sediment from basal erosion and bank failure are considered as source terms for sediment continuity, and then advance or retreat of bank lines are determined by solving the near-bank mass conservation equation. The present model adopts a simple bank-failure model similar to the slumping bank-failure model.

Basal erosion

Basal erosion entrains bank material under the water surface. The rate of basal erosion is the rate of bank material entrainment to the water body per unit channel length per unit time. The depth-averaged bank erosion rate is decided as the difference between the entrainment and deposition of bank material expressed as follows in Duan(2001)

$$\xi = sin\bar{\beta}\sqrt{\frac{C_L}{3\rho_s}}\left(1-\frac{C}{C_*}cos\bar{\beta}\right)\left(1-\frac{\tau_{bc}}{\tau_{b0}}\right)^{\frac{3}{2}}\sqrt{\tau_{b0}} \tag{34}$$

where $\bar{\beta}$ is the averaged bank slope; $\bar{x}$ is the depth-averaged bank erosion rate due to hydraulic force; concentrations C and C_* are the depth-averaged and equilibrium concentrations of suspended sediment, respectively, such that $C = C_*$ for equilibrium suspended load transport; ρ_s is the density of sediment particle; C_L is the coefficient of lift force ranging from 0-1 to 0-4 depending on the mean grain size of the sand (Chien and Wan, 1991); shear stresses at the toe of the bank slope and critical shear stress for basal erosion are represented as $\tau_{bo}$and τ_{bc}, respectively. Shear stress at bank toe equals the shear stress acting on the channel bottom, τ If bank material is the same as bed material, such as in Friedkin's (1945) experiment, the critical shear stress of bank material has the same value as that for bed material.

The mass volume contributing to the main channel from basal erosion can be calculated as

$$q_{br}^{b}=\frac{\xi(1-p)h_b}{\sin\beta} \tag{35}$$

where q_{br}^{b} is the net volume of sediment contributed to the main channel from bank erosion, and h_b is

flow depth at near-bank. To account for the porosity p of the bank material, the factor 1 - p is multiplied at the denominator. If $\xi = 0$, the riverbank is not undergoing erosion, so the near-bank, suspended sediment concentration reaches the value of equilibrium. The term $\sin\beta$ converts the distance of bank erosion to the volumetric net bank material from basal erosion.

Mass failure for non-cohesive bank material

Pizzuto (1990) applied a slumping bank-failure model for non-cohesive bank material, which was later modified by Nagata *et al.* (2000). Fluvial erosion degrades the channel bed and destabilizes the upper bank until the bank angle exceeds the angle of repose for bank material. The slumping bank-failure model requires the bank-failure surface to be inclined at the angle of repose projected to the floodplain. It is well suited for the case of non-cohesive sediment, like the laboratory experiments of Friedkin (1945) and Lan (1990).

In natural conditions, vegetation, heterogeneity in bank and water pressure pore will increase an apparent cohesion to the original non-cohesive material. The planar bank-failure model (Osman and Thorne, 1988; Darby and Thorne, 1996) is more appropriate as compared to the slumping model. In this paper, the slumping bank-failure model was combined with the parallel retreat method. It presumes that mass wasting from bank failure is the result of the rate of basal erosion and height of the bank surface above the water surface. As such, the amount of bank material from mass failure is estimated as

$$q_{br}^{f} = \bar{\xi}\Delta h_{bank}(1-p) \tag{36}$$

where q_{br}^{f} is the sediment material eroded per unit channel width from bank failure, and $\xi\Delta h_{bank}$ is the bank height above the water surface.

Advance and retreat of bank lines

Bank erosion causes bank advance or retreat. An advance is resulted by the sediment deposition near the bank. The deposited sediment can be moved from an eroded bank or bed material shifted from upstream. A bank retreats as the material is transported away by flow. Predicting bank advance or retreat is based on a balance (or mass conservation) of the sediment in a control volume near the bank, including sediment from bank erosion and failure, sediment stored on the bed due to deposition, and sediment fluxes transported in and out of the control volume. Considering the mass balance within a control volume near the bank (Figure 1), the sediment continuity equation is written as

$$\left(q_l + \frac{\partial q_l}{\partial l}dl\right)\frac{dr}{2} - q_1\frac{dr}{2} + q_r dl - q_{br}dl = -\varepsilon h_b dl \tag{37}$$

where ε is the actual bank erosion rate; $\varepsilon > 0$, $\varepsilon < 0$, and $\varepsilon = 0$ correspond to bank advance, retreat, and unchanged, respectively; and dr is the width of the control volume (Figure 1). Simplifying and eliminating $dl$and dr from both sides of Equation 37 produces

$$\varepsilon = -\frac{\left(\frac{\partial q_l}{\partial l}\frac{dr}{2} + q_r - q_{br}\right)}{h_b} \tag{38}$$

where ε is the bank erosion rate (if the bank advances, $\varepsilon > 0$; if the bank retreats, $\varepsilon < 0$; if the bank is unchanged, $\varepsilon = 0$); dr is defined as the width of the control volume nearest to the edge of the bank; h_b is

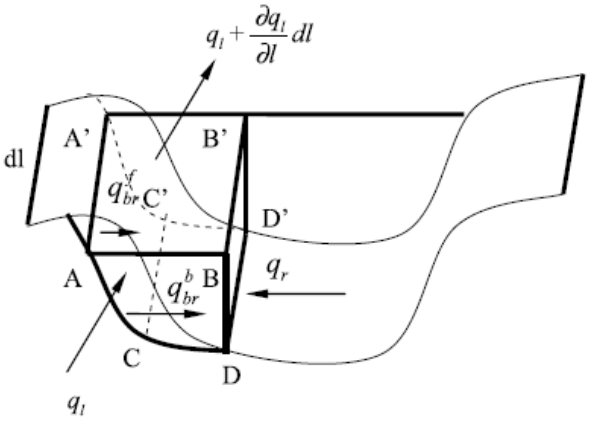

Figure 1. Mass balance at near-bank region.

the near-bank flow depth; q_l and q_r are the total sediment transport rates in the longitudinal and transverse directions, respectively; and $q_{br} = q_{br}^b + q_{br}^f$is the transversal component of the sediment transport rate at the near-bank region as a result of bank erosion. Under the assumption of a triangular cross-section of the boundary element, *dr* in Equation 38 is half the distance from the nearest boundary node to the edge of bank. One can reason from Equation 38 that the bank retreats when the net longitudinal and transverse sediment transport rate is decreased or a net amount of sediment materials are carried out of a control volume near the bank. Conversely, if the net sediment transport to the control volume is increased, the bank will advance. The variable *dr* is defined as the width of the control volume adjacent to the bank.

Comparing with the bank erosion model of Ikeda *et al.* (1981), the present rate of bank erosion is decided by the flow and sediment conditions near the channel bank rather than by only excess velocity. As per the movement of a bank is only related to the near-bank flow field. If the excess near-bank velocity is greater than zero, the bank will retreat. Equation 38 considers sediment transport fluxes, and one can see that even when flow velocity and shear stress near the bank are high, the bank may not retreat, because a net sediment flux may be transporting into the control volume adjacent to the bank.

Numerical Methods

The 'efficient element method' (Wang and Hu, 1990) is applied to solve the momentum and continuity equations. The numerical technique was originally a collocated, weighted residual finite element method. The traditional Lagrangian interpolation function is employed to discretize the linear terms in Equations 1, 2, and 3. To address adequately the upwinding effect, another set of interpolating functions is derived based on the solution of the convection and diffusion equation to discretize non-linear terms (advection terms) in the flow momentum equations. These two sets of shape functions are transformed to the shape function for global elements based on the isoparametric mapping approach. A detailed description of the numerical scheme for the flow hydrodynamic model can be found in Duan (2004).

The sediment continuity equation (Equation 33) is discretized using the Lagrangian interpolation shape functions. A backward finite difference scheme is used for the time derivative term. The discretized form of Equation 33 is

$$(1-p)\frac{z_b^t - z_b^{t-1}}{\Delta t} + \sum_{i=l}^{9} \frac{\partial \varphi_i}{\partial x} q_{xi} + \sum_{i=l}^{9} \frac{\partial \varphi_i}{\partial y} q_{yi} = 0 \qquad (39)$$

where φ_i is the shape function with the superscription denoting the time step, and the subscription denoting the node number. In the present study, flow and bed deformation computations are decoupled. Sediment transport rates are calculated after flow has reached a steady state. Then, Equation 39 is solved to obtain a new bed elevation. The time step of sediment computation is selected such that bed-elevation changes are less than 2 per cent of the flow depth.

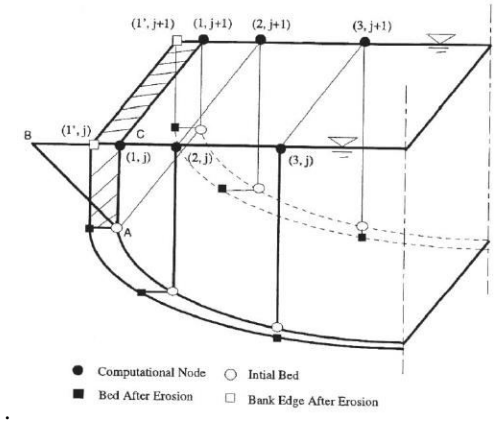

Figure 2. Movement of nodes at banks

In order to calculating bed-elevation changes in Wainganga r bank lines are also adjusted as per the rate of bank erosion. Figure 2 exhibits the calculation with Equation 38 for the bank advance and retreat rate at the elements near to the bank. The boundary nodes are *(1 , j)* and (1, j + 1), and the nearby internal nodes are (2, j) and (2, j + 1). Equation 38 is solved at node (1, j) to obtain the bank erosion rate at the edge of bank B. The boundary element used to evaluate the bank erosion rate is a prism-like, three-dimensional element with a triangular cross-section *ABC*. The bank erosion rate at node (1, *j)* is assumed to be the same as that at the edge of bank B, which can be expressed as

$$\varepsilon_{i,j} = \frac{\Delta r}{2}\frac{q_1(2,j)-q_1(2,j+1)}{\Delta l} - q_r(2,j) + q_{br}(1,j) \tag{40}$$

where Δr is the distance between *B* and C. As a boundary condition, the longitudinal component of the sediment transport rate at node (1, j) is assumed to be the same as the adjacent internal node (2, j). Using Equations 35 and 36, the expression $q_{br}(i,j) = q_{br}^{b}(i,j) + q_{br}^{f}(i,j)$is calculated. According to the bank erosion rate, each boundary node is moved the distance of $\Delta B_{1,j}$

$$\Delta B_{1,j} = \varepsilon_{1,j}\Delta t_{bank} \tag{41}$$

where Δt_{bank} is the bank erosion time step. In Figure 2, (1', j) and (1', j + 1) are the boundary nodes after bank erosion, and the hatched area represents the eroded material. At the inlet section, the bank erosion rate is assumed to be zero. At the outlet section, the bank erosion rate is assumed to be the same as in the adjacent upstream section.

Mesh-adjustment algorithm

During the research of Wainganga River, the erosion distance at each boundary node, the new boundary lines (dark solid line in Figure 3) are obtained. Since the boundary of the computational domain is changing, the mesh must be adjusted from time to time. The dynamic mesh traces the boundary of the meandering channel and matches the computational domain to the new channel. The new mesh for the next time step is equally spaced along the banks and is also equally spaced in the transverse direction.

In Figure 3, open dots denotes the old boundary nodes, and solid dots denotes the boundary nodes after the river banks are moved according to the erosion distance. Solid squares denote the boundary nodes after the mesh is adjusted. In this figure, node *A* retreats, and node *B* advances. The old cross-section *AB* is moved to *A'B'* after bank erosion occurs. Assuming that the channel width remains unchanged during the meandering process, bank retreat at one side of the channel should be equal to the

advance at the other side of the channel. In these channel-meandering simulations, the bank erosion rate is the average of the rates at both banks of the channel because a constant channel width is assumed.

The new centreline is obtained by connecting the centres of each new cross-section. For example, the centre of cross-section *A′B′* is the point *C′*. The new centreline may be somewhat longer or shorter than the previous centreline due to deformation of the meandering loops. Because no additional nodes are added or deleted during computation, the position of each cross-section should be relocated to obtain a mesh for better computational accuracy and efficiency. The new centreline is equally divided, and the centre of each cross-section is relocated. For example, the dashed line in Figure 3 represents the new centreline. Open squares represent the centres of the new cross-sections after the equal division. *C*" is the new centre of the old cross-section *AB*. Points *C* and *C″* are usually quite close because the bank is only restricted to move a distance of lessthan 2 per cent of the channel width at each time step. In the case of a high erosion rate, the time step of bank erosion must be reduced. The adjusted cross-section *A″B″* must be normal to the new centreline at *C″* and have a width equal to the initial channel width AB. Then, for each cross-section, computational nodes along the transverse direction are uniformly distributed. The adjusted mesh has the same computational domain as the previous one, even though the positions of cross-sections and computational nodes have been relocated in the physical domain. Each new cross-section of the adjusted mesh is normal to the new centreline, and computational nodes are uniformly distributed along the transverse direction. Since the computational nodes do not move considerably in each time step, bed elevation at any node in the new mesh is interpolated according to the bed elevation of the adjacent upstream and downstream nodes in the old mesh. After the mesh is adjusted, the flow field must be recalculated for a certain time to achieve a steady state in the new channel. This entire process is repeated for each new morphological time step until the simulation is completed at the specified time step. Since boundary nodes move less than 2 per cent during each time step, the error due to interpolation is assumed negligible.

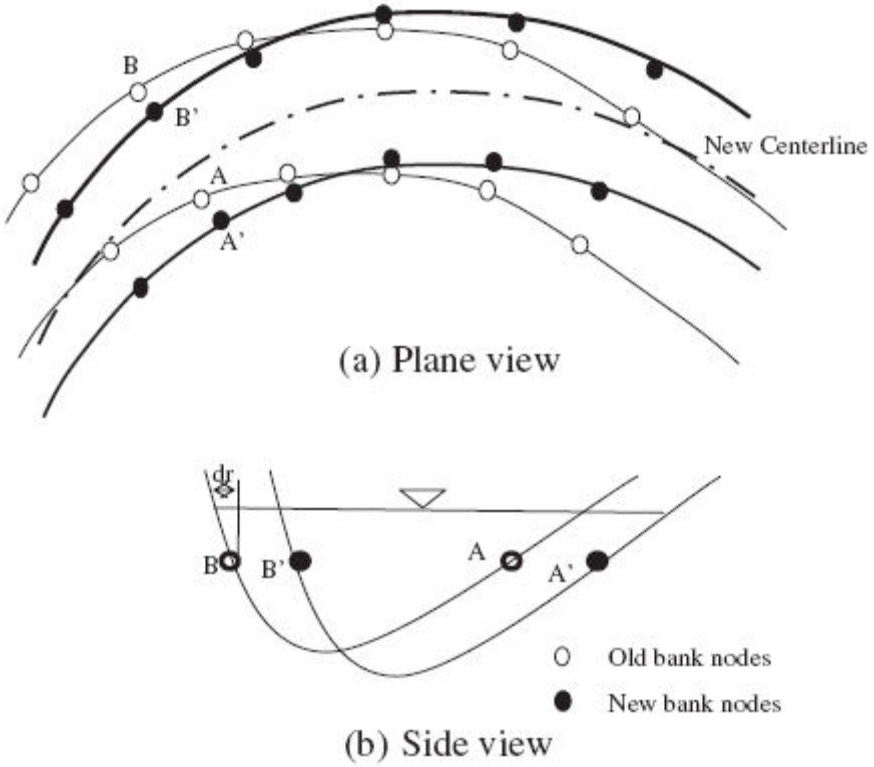

Figure 3. Adjustment of channel boundaries.

Test and Verification

Series of experimental studies observed by Friedkin (1945) to examine the processes, due to which meanders are formed, and the relationships of meander formation to water discharge, sediment load, bank composition and valley slope. In the current study, the Friedkin (1945) experimental case involving initiation of the meandering process was simulated where a straight channel having a single meandering loop at the inlet was developed into a meandering channel. In his experiment, a constant discharge of 1-416 $^{l}/_{s}$ was introduced at the inlet. The initial cross-section was trapezoidal with a top width of 25-96 cm and a bottom width of 17-37 cm. About one-third of the initial bend had a non-erodible rigid wall. Bed sediment was relatively uniform with a mean size of 0-45 mm. Bank material and bed material were uniform, homogenous, and non-cohesive. After three hours, a meandering channel was formed (shown in Figure 4). The results were repeated in a subsequent run where the same number of meandering loops having similar magnitude and wavelength were produced.

In this simulation, a two-dimensional, computational mesh is generated for the original planform. Flow discharge is indicated as a constant at the inlet. The discharge of suspended and bedload sediment at the primary section is equal to the transport capacity of bedload and suspended load. The boundary roughness height equals the mean particle size, and the water surface elevation at the outlet cross-section remains constant. For the simulation, the banks of the upper third of the first bend are fixed. The outlet cross-section is set parallel to the immediate upstream cross-section, allowing the outlet cross-section to rotate around its centreline. In this simulation, a constant channel width is maintained by averaging the rates of bank erosion at both banks.

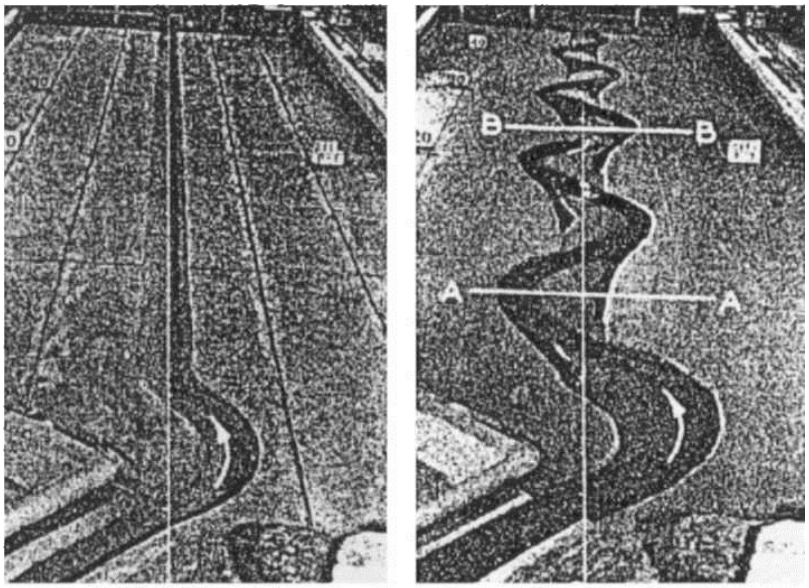

Figure 4. Photo of experimental result.

In Figure 5; Adjustments to the computational meshes made during the simulation are plotted. The top diagram explains the original mesh, and the bottom one explains the mesh of the fully developed meandering channel. The present model needs the total number of cross-sections and nodes in each cross-section to remain unchanged, so the distance between cross-sections increases as the channel length increases. In this model run, the initial aspect ratio of the finite element mesh is 1:4, and the aspect ratio of the developed meandering channel is 1:7, which satisfy the convergence criteria for the hydrodynamic model (Duan, 2004). After each mesh adjustment, the flow field is recalculated as the initial condition by using flow solutions from previous time steps

The simulated flow field is drawn in Figure 6. It consists the flow velocity vector, and surface

elevation occurring during the meander-forming process. The flow depth is too shallow, and velocity is low in areas outside the computational reason; consequently, the present model presumes that sediment transport in these areas is too less. At the beginning of the simulation (T = 0 h), the initial meandering loop causes a redistribution of flow momentum. As time progresses, sand bars develop near the inner bank of the initial loop and at the location where the initial loop connects with the straight reach. At T = 0-5 h the primary flow course becomes wave-like because sand bars form in the straight reach. This wave-like flow pattern facilitates the development of sand bars, and at T = 2-0 h, a fully developed meandering loop occurs in the straight reach. Two additional meandering loops are fully developed at T = 3-0 h.

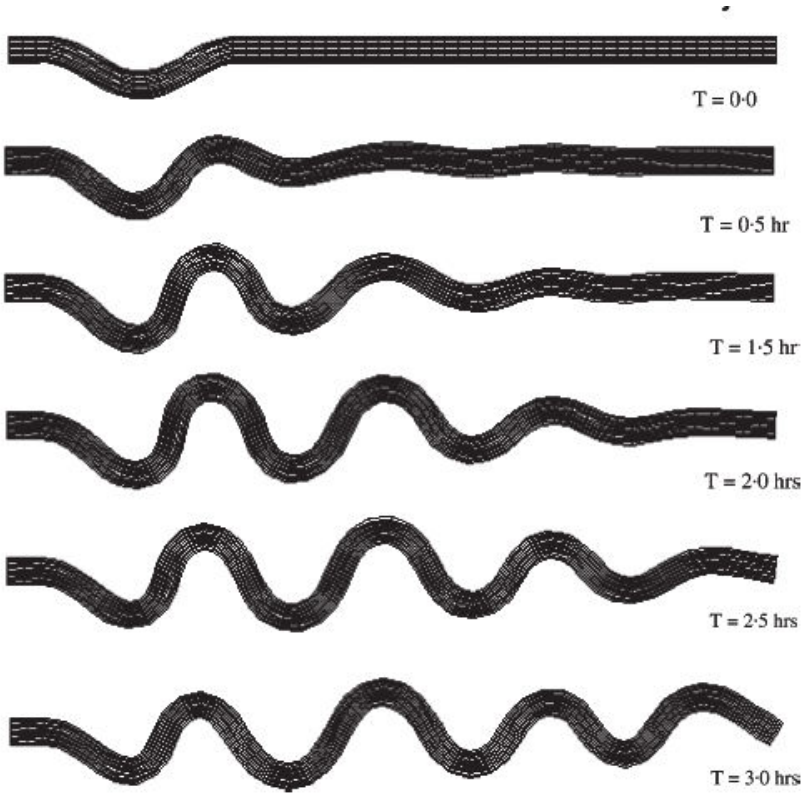

Figure 5. Changes in computational meshes during the meander-forming processes.

Near the inner bank at the beginning of the simulation, high-velocity zones are observed. The velocity zones gradually shift to the outer bank as the transverse bed slope increases due to the presence of sand bars. Parker (1984) and Dietrich and Smith (1983) attributed this phenomenon to the secondary flow generated by bed topography. Simulation results indicate that the initial meandering loop propagates downstream through the formation of sand bars, resulting in a meandering flow path. Apparently, because of the uniform bed and bank material, the initial bend can be transmitted almost perfectly downstream, producing a series of uniform bends. After the meandering process reaches equilibrium, a series of almost identical sand bars resides on the inside of bends.

The simulated bed elevations for the various stages in the meandering process are drawn in Figure 7. Simulation results show that the generation of alternate bars occurs at both sides of the channel and the inception of channel meandering after the alternate bars are formed. With the progresses of time, the meandering amplitude and wavelength increase gradually. Friedkin (1945) states that bends develop as flow impinges on the bank and erodes bank material, then deposits the material on the inside of the bend. Super-elevation on concave banks of this low-sinuosity stream is observed in the experiment

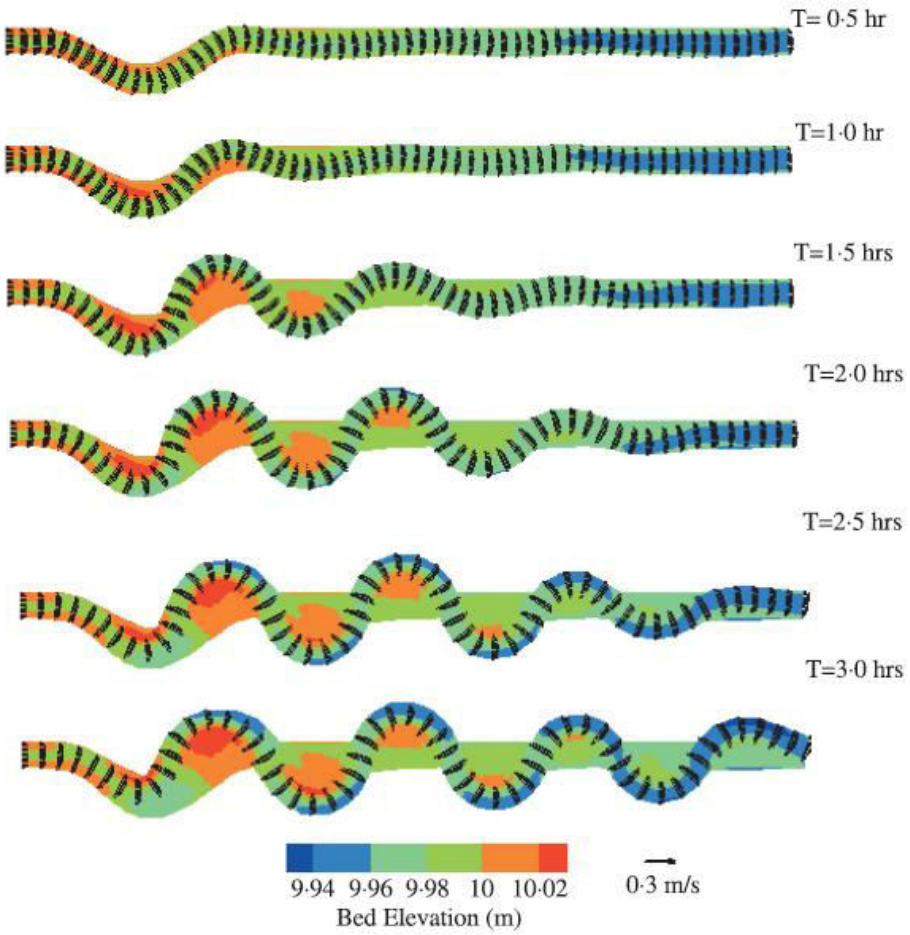

Figure 6. Simulated flow field including velocity and surface elevation.

Super-elevation of flow near the concave bank increases as the meandering process evolves, indicating that secondary flow becomes stronger as sinuosity increases. The amplitude and wavelength of the formed meandering stream are very close to experimental observations as shown in Figure 4.

Meander channel evolution

Neither laboratory experiments nor field measurements are able to record through real-time measurements the detailed history of meandering channel evolution. By contrast, a numerical model can record the planform evolution changes of meandering channels, as well as the flow topography and momentum, at each time step. Therefore, the simulated entire evolutionary process was divided into five phases according to the characteristic changes in meandering planform geometry

1. At the early stage, a near-straight channel migrates rapidly in the downstream direction.
2. As sinuosity increases, downstream translation diminishes and meandering loops expand laterally in the second stage.
3. When sinuosity is sufficiently large, the rate of downstream migration reduces and the planform geometry remains essentially unchanged for some time.
4. Meandering loops migrate in the upstream direction and continue to expand laterally.
5. As channel sinuosity continues increasing, the meandering loops begin to rotate until reaching a sinuosity about 3.7. Consequently, a neck cutoff will be formed.

The meandering planforms are found in natural freely meandering rivers. 8 showed five reaches of a free meandering river in upper Wainganga river valley in Balaghat district can be traced from Google Earth. Figure. 3, which indicated different reaches of this river are at various stages of meandering evolution. At

stages 4 and 5, bifurcation occurred that will further complicate the meandering evolution process. The current model version cannot simulate the process of a neck cutoff. Correlations between the rate of bank erosion with flow momentum and bed elevations at different stages of meandering evolution are described in the following sections. In the following sub-sections, each phase of the channel development process is illustrated with changes in bed elevation and with the corresponding distribution of momentum over the reach.

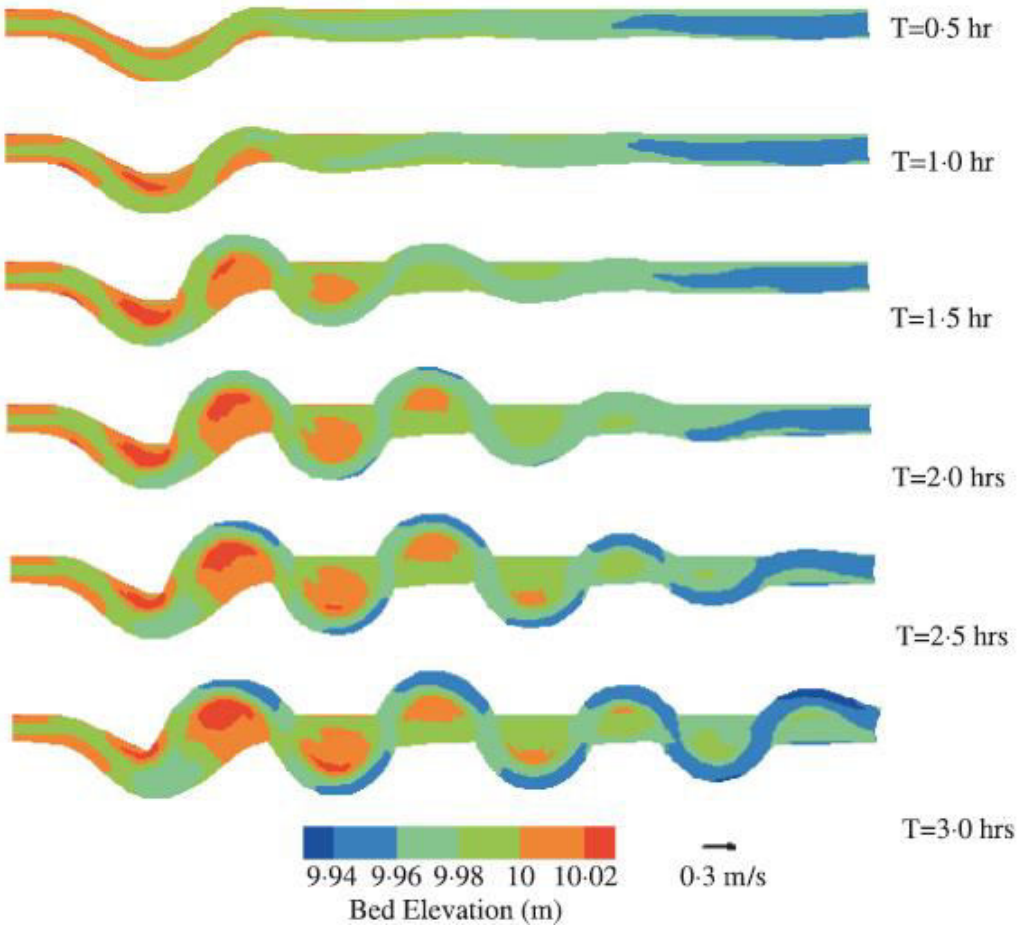

Figure 7. Initiation of a meandering channel from a straight channel.

Phase 1: downstream migration

This phase is characterized by downstream translation and slight rotation of meandering loops. Fig. 9a and b is the bed topography and the momentum distribution of the initial sine-generated meandering channel, respectively. 10a, shows that the meanders migrate downstream, when channel sinuosity is low (less than 1.4). The head of the first meandering (bend #1) loop slightly rotates downstream until sinuosity reaches 1.4. As the meandering loop migrates downstream, large sediment deposits or point bars (marked in red) shown in 10a, emerge on the convex bank near the apex. They expand almost symmetrically to the apex with a slight rotation in the downstream direction. 10 b shows the distribution of flow momentum, or unit discharge defined as the product of velocity and depth, in shaded colors. This figure shows

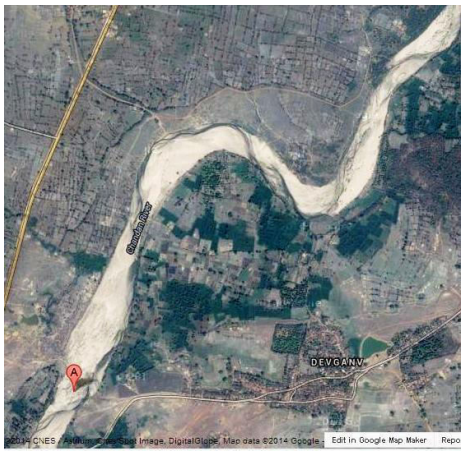

Stage:1 downstream Translation

Stage:2 Lateral Extension

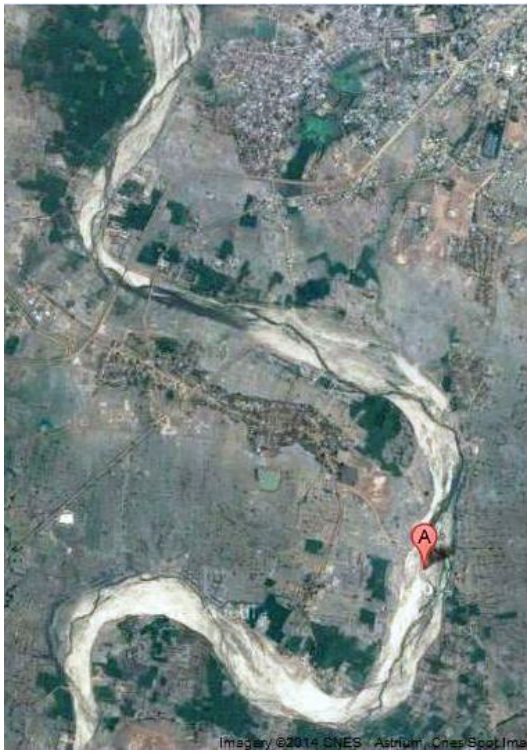

Stagte3: Relative stable

Stage4: Lateral Extension

Stage 5: Final Stage near cuttoff

Figure 8. One free meandering river in Wainganga Valley .

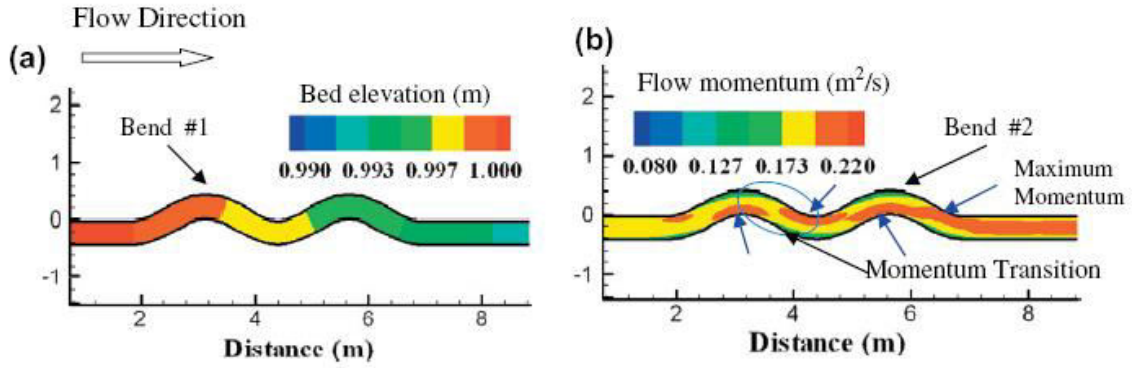

Figure .9 Initial sine generated meandering channel (black *T=0* g.)

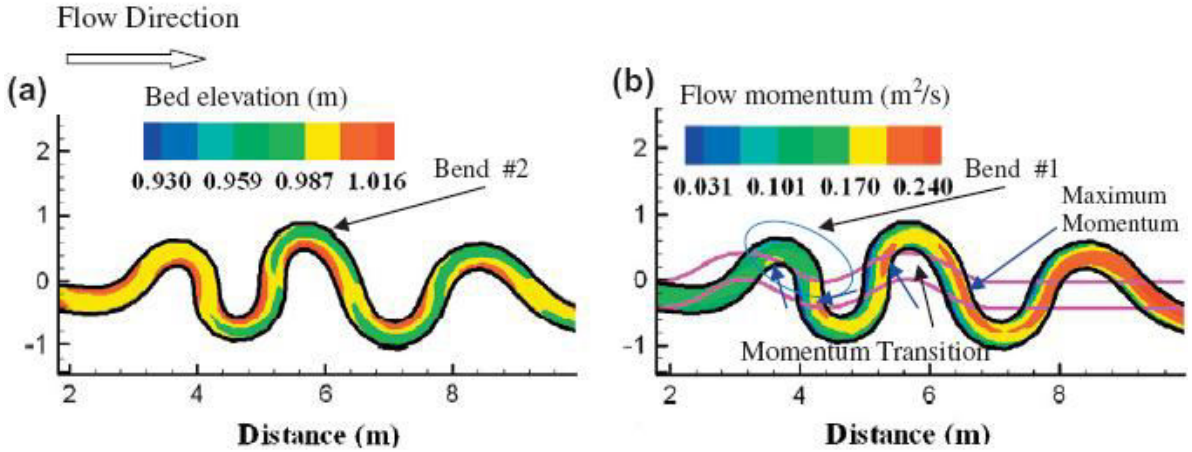

Figure 10. First phase of downstream meandering migration (black, *T = 1.5* h, purple *T = 0* h).

that the maximum momentum zone resides near the convex bank in the region upstream of the apex pointed by the blue arrow. Sand bars form where flow momentum is reducing in the downstream region of the apex. The location where the maximum momentum shifts from the convex bank (or the inner bank) to the concave bank (or the outer bank), hereafter is called the momentum transition zone, occurs slightly downstream from the apex as shown in the first bend (marked in a blue ellipse)

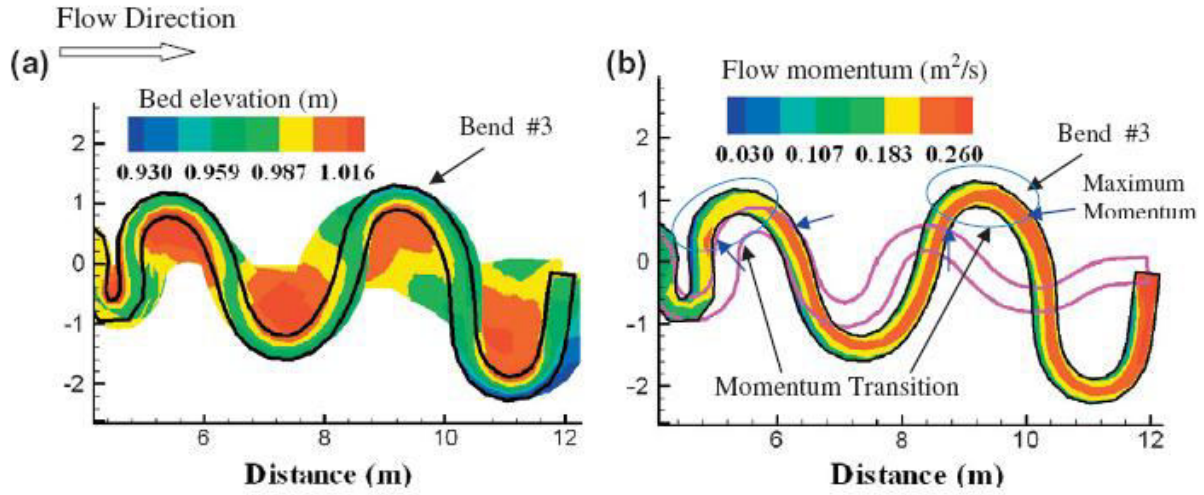

Figure 11. Second stage of lateral expansion (black *T* = 6.0 h, purple *T* = 1.5 h).

Phase 2: lateral extension

11a shows the evolution of bed topography especially the growth of point bars during the processes of lateral expansion. When channel sinuosity is larger than 1.4, downstream migration reduces, while lateral extension increases appreciably at both the second and the third bend. When meandering loops extend laterally, the head of the loop slightly rotates in the upstream direction at the second bend and in the downstream direction at the third bend. As a consequence, sand bars expand laterally while tilting to the downstream or upstream directions that correspond with the directions of head rotations. Changes in distribution of flow momentum shown in 11b explain why the lateral expansion replaces downstream translation during this second phase. Sand bars form where flow decelerates and flow momentum begins to decrease. On the concave bank, the maximum momentum zone (pointed by a blue arrow) resides close to the inflection point at the second bend, while it is located upstream of the inflection point at the third bend. Therefore, in the second bend, flow is accelerating at the concave bank until reaching the maximum momentum at the inflection point. This flow acceleration will cause bank erosion. This acceleration zone also exists at the concave bank in the third bend, but has a shorter length than that in the second bend. This distribution results in a longer reach subject to bank erosion due to flow acceleration on the concave bank in the second bend that perhaps drives the head rotates toward the upstream. Consequently, the second bend rotates towards upstream, but the third bend towards the downstream.

On the other hand, at the second bend, the meandering loop rotates in the upstream direction when the momentum transition zone is located at the immediate upstream region of the apex. At the third bend, the meandering loop rotates in the downstream direction as it extends laterally where the momentum transition zone is located at the downstream of the apex. Therefore, the location of the flow momentum transition determines whether the head of a meandering loop is rotating downstream or upstream as it migrates downstream and extends laterally. Not only the geometry of the meandering planform but also the topographic features (e.g., point bars) affect the redistributions of flow momentum in meandering channels. Without the formation of point bars, the maximum flow momentum always resides close to the inner banks (9b), so that meandering channels will not evolve into high-sinuous meandering channels (Chen and Duan, 2006). The point bar formation redistributes flow momentum and causes the momentum transition zone shift to near the apex. As a result, the migration of meandering channels is dominated by the formation of point bars, as well as by the evolution of meandering plan-forms. The sinuosity of a meandering loop is about 2.0 in this phase.

Phase 3: quasi-equilibrium

A quasi-equilibrium meander in (Fig.11) a indicates that the plan-form geometry of the meander loop remains almost unchanged when the meandering loop has a sinuosity of 2.0. During this phase, the rate of lateral bank erosion is negligible, and therefore
the planform of the meandering loop does not change for about 8 h. (Fig.11) a shows a nearly symmetrical meandering loop, and the transition reach in the upstream and downstream regions of the bend is perpendicular to the flow centerline at the apex. Additionally, the point bars continue to grow at a slow rate, and the growth of sand bars is almost symmetrical with respect to the apex. (Fig.12) shows that the flow momentum is lower and more uniformly distributed than in the first two phases. The maximum flow momentum is located near the convex bank close to the crossing and then move towards the apex of the meander bend as meandering evolves (Fig. 13). Because of the symmetrical meandering planform and size and geometric location of sand bars, the migration rate of this meandering planform is almost zero although point bars continue to grow and the distribution of flow momentum continues to change slowly.

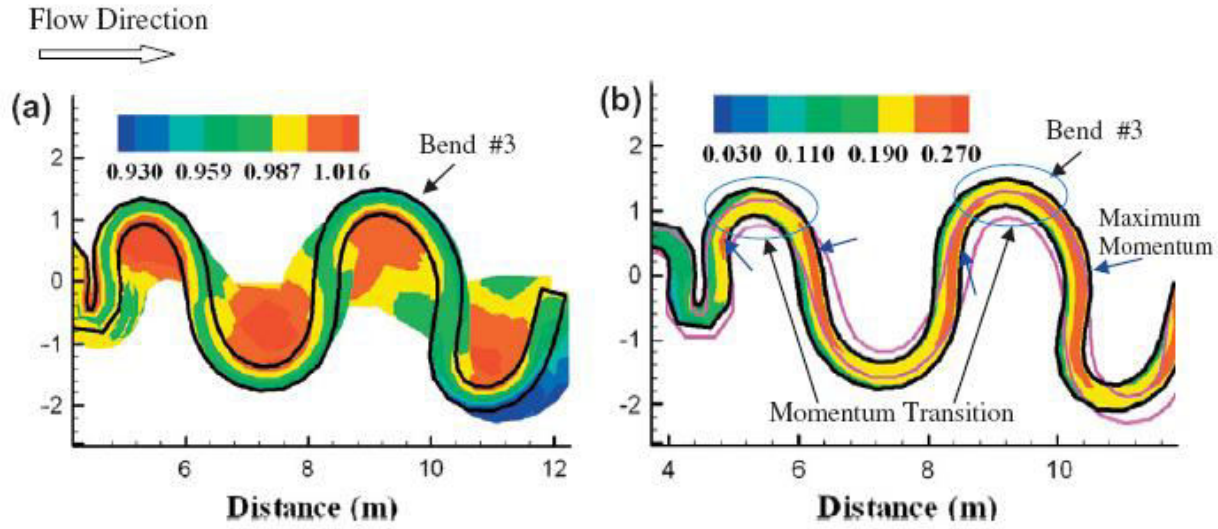

Figure 12. Third stage of meandering migration of quasi-equilibrium (black T = 20 h, purple T =12 h).

Phase 4: upstream migration

As point bars grow larger (Fig. 13), the maximum flow momentum zone in the upstream half of the bend shifts toward the apex, while the maximum flow momentum zone in the downstream half of the bend moves past the crossing (Fig.13). Since flow momentum in the downstream half of the bend is larger than in the upstream half, the entire meandering loop begins to migrate in the upstream direction. The purple line in denotes the channel boundaries at T = 20 h, and the black line denotes the channel boundaries at T = 26 h. The meandering loop also expands laterally as it migrates in the upstream direction. Since the maximum momentum zones reside near the crossing and the momentum transition zone is located almost at the apex, the meandering loop remains symmetrical as it migrates in the upstream direction. Although no upstream or downstream rotation is observed, the neck of the meandering loop becomes narrow, which indicates that the rate of migration at the downstream crossing is greater than at the upstream crossing.

Phase 5: meandering channel rotation

As soon as the maximum momentum zone shifts toward the apex, the momentum transition zone moves to the downstream region of the apex (Fig.14). Therefore, the head of the meandering loop begins to rotate in the downstream direction, and its migration rate in the upstream direction begins to reduce. Fig. 12 a shows that asymmetrical point bars are starting to develop with a lobate feature pointed in the

downstream direction. The purple lines in (Fig. 14) are the boundaries of the meandering channels at T = 26 h, while the black lines are the boundaries at T = 32 h. Notice that these features take a long time to develop compared to Phases 1 and 2. This is because the sinuosity is very high and the momentum is much lower than in Phases 1 and 2. Since the crossing reach in the downstream half of the bend migrates upstream faster than that in the upstream reach and because the head of meandering loop rotates in the upstream direction, a goose-neck shaped meandering loop is formed. This goose-neck shaped meandering loop is a very common planform in natural meandering streams where some bends have a head in the upstream direction and some have a head in the downstream direction. It has been observed that 40% of Wainganga River bends have their heads toward the downstream direction and 60% toward the upstream

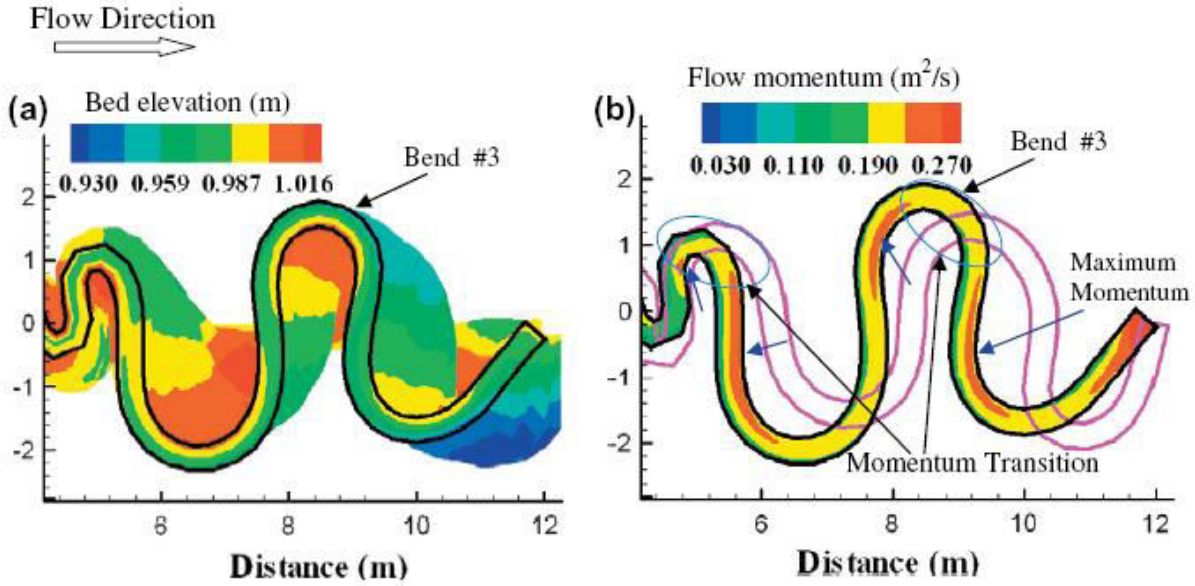

Figure 13. Fourth stage of upstream meandering migration (black T = 26 h, purple T = 20 h).

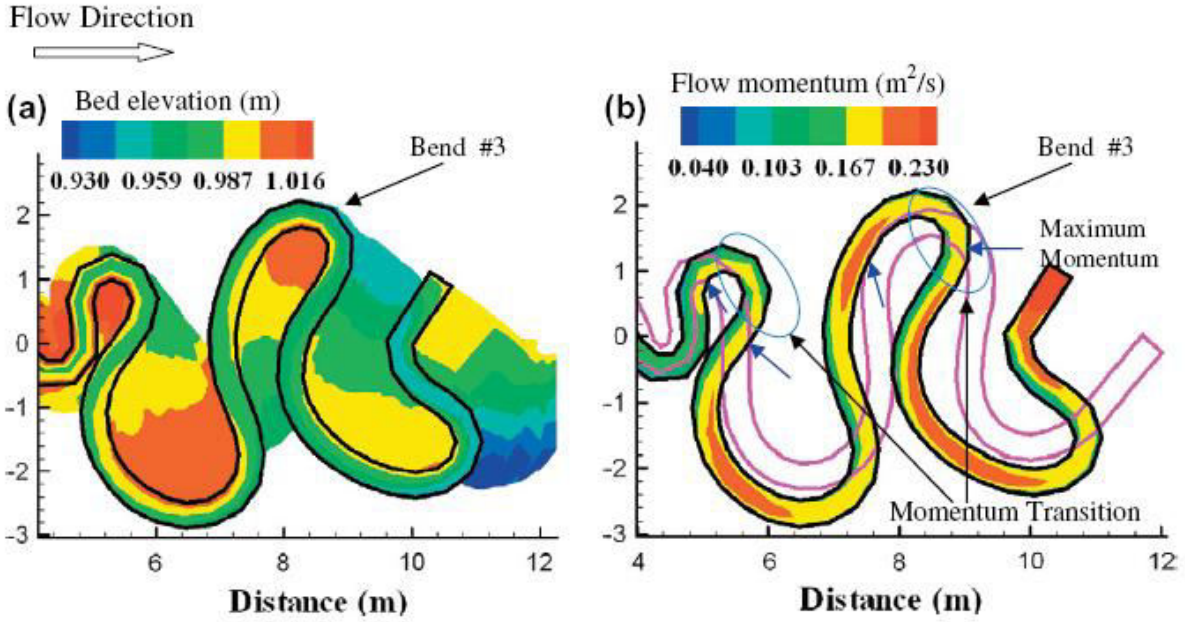

Figure 14. Fifth stage of rotation and meandering migration (black T = 32 h, black T = 26 h).

direction . Whether the head of the meandering loop is upstream or downstream depends on the location of flow momentum transition zones. This simulation through the present study indicates that if the momentum transition zone is located exactly at the apex, the meandering loop will expand only laterally. However, if the momentum transition zone is located immediately upstream from the apex, the meandering loop will migrate and rotate in the upstream direction. Otherwise, the meandering loop will migrate and rotate in the downstream direction.

In summary, the evolution of a meandering channel begins with downstream translation and is followed with lateral expansion, and upstream/downstream rotation before it reaches a quasi-stable state where sinuosity is approximately 2.0. The quasi-stable meandering planform has a minimum bank erosion rate, and the meandering planform is almost symmetrical with respect to the apex. When sinuosity in a meandering channel slowly continues to increases, the quasi-steady meandering planform migrates in the upstream direction and continuously expands laterally. The upstream migration rate eventually decreases and the head of the meandering loop rotates in the downstream direction. A goose-neck shaped meandering loop is formed at end of the simulation.

This evolution process of the meandering planform geometry is closely linked to the distribution of flow momentum, especially at the location where the maximum flow momentum zone shifts from one bank to the other. The simulated results indicate that the location where the maximum momentum zone shifts from the convex to the concave bank in a meandering channel varies with strength in the secondary current, which is induced by the curvature of meanders and the transverse bed slope due to the development and expansion of sand bars. Laboratory experiments (Friedkin, 1945; Schumm et al., 1987) have also shown that a meandering channel can evolve from a mildly curved channel to a highly sinuous channel. As soon as a sinuous channel develops, the transverse slope appears with the accompanying formation of sand bars. The core of the maximum momentum zone moves to the center and then to the concave bank due to the increased curvature and topographically induced secondary flow. This influence of topographically induced secondary flow is believed to be at least as important as secondary flow induced by curvature (Hooke, 1975; Dietrich and Smith, 1983; Dietrich and Whiting, 1989; Nelson and Smith, 1989).

Natural meandering channels have different planform configurations and various types of sand bars (e.g., point bars, multiple bars). The location of the maximum momentum zones and the transitions of momentum from convex or concave banks may occur anywhere within a meandering bend. This momentum shift determines if the evolution of a meandering channel is downstream/upstream translation, lateral expansion, upstream/downstream rotation, or any combination of these motions. The presence of developed sand bars near the convex bank in highly sinuous channels causes a large transverse slope, which facilitates the shift of the maximum shear stress zone to the concave bank.

Discussion

An example from the Wainganga River in Balaghat district in Madhya Pradesh, India is shown in (Fig.15, 16 and 17). Accordingly, a straight channel was excavated with a vertical drop (about 2 m) in sandstone in order to prevent lateral migration and eventual impingement of the channel into the nearby road embankment. The elevation drop triggered a slight lateral perturbation of the system and the downstream portion of the channel started to meander. The features of the channel shown in (Fig.15 16 and 17) are quite similar to the features obtained by the model. Essentially, the amplitude of meandering decreases in the downstream direction. The resulting channel features are very similar to those described by the model in Figure 7.Natural meandering streams generally have cohesive banks (Knighton and Nanson, 1993; Millar, 2000).

Figure 15. The formation and evolution of meandering in Bajrang Ghat, Balghat both process and physically based bank erosion and meandering are feasible.

Figure 16. The physically based image calculates a sediment transport and bank erosion to determine the advance and retreat of channel bankline. This is a specific location in natural meander from hills of Balaghat

Figure.17: Wainganga River specifically denotes the image to determine the rate of bank erosion at individual location after Dhuti dam within a natural meandering channel by knowing the flow field bank geometry and bank material. This expected more successful in predicting immediate Geomorphic response to river modification

Retreat of cohesive bank lines is a complex process consisting of fluvial erosion, bank failure, weathering, piping or sapping. Bank failure can dominate bank erosion processes involving cohesive bank material, and algorithms for mass failure are available for cohesive banks (Darby and Delbono, 2002). Bank failure models for cohesive bank material, such as planar models (Osman and Thorne, 1998; Darby and Thorne, 1996), rotational models or cantilever models, can be used inplace of Equation 36. Bank failure is a probabilistic phenomenon with a frequency relating to the frequency of river flood flow that can be approximated with a LP(3) distribution (Duan, 2001). The mass volume from bank failure is estimated as a function of bank geometry, properties of bank material, and frequency of bank failure.

Conclusions

This study incorporates the physically based bank erosion model into the mass conservation equation to forcast the rate of bank line advance or retreat. The bank erosion model combined with a two-dimensional hydrodynamic model replicates Friedkin's laboratory experiments on the formation of meandering streams. An important aspect of this model is that bank erosion does not guarantee the retreat of a bank line if eroded bank material remains at the toe of the bank. Whether or not a bank retreats or advances depends on the balance of sediment load at near-bank regions where sediment may come from upstream, bank erosion, and secondary flow. The strength of secondary flow in redirecting bedload transport correlates with the local radius of curvature as well as sinuosity of meandering channels. Modelling results clearly demonstrated the evolution of meandering from perturbation. The resulting meandering channel has almost uniform loops, and the location and size of the sand bars are similar to the

experimental observations. The essential processes leading to meander formation are well replicated with this model. Additionally, modelling results also indicated that suspended sediment is less important in modelling meander migration, while bank erosion and bedload transport play significant roles in the meandering evolution process. The growth of sand bars determines the hydrodynamic flow field that pushes towards the concaving banks. Bank material from the caving banks will supplement sediment deposits on point bars when bed and bank material are the same, such as in the laboratory experiments. At this point, this model properly simulates key laboratory experiments of channel meandering. It is also very similar to some features observed in the field, such as observed on the Wainganga River(Dongre NL,1979) in India. This model enhances the current capability in modelling natural morphodynamic processes. This also contributes to better understanding of the processes of lateral channel migration and helps explain the formation of river meanders.

The primary conclusions of this study are: (1) this 2D numerical model clearly demonstrates the evolution of meandering channels from low to high sinuosity; (2) the growth of point bars affects the distribution of shear stress, secondary currents and flow momentum; and (3) the model properly simulates the various modes of deformation of meandering channels, such as downstream and upstream migration, lateral extension and rotation of meander bends. The essential processes leading to formation of meandering channels are well replicated with this model. The modeling results contributed to better understanding of the processes associated with lateral channel migration, as well as aids in explaining the formation of river meanders.

References

- ASCE Task Committee. 1998. River width adjustment. I: Processes and mechanisms. *Journal of Hydraulic Engineering* **124**(9): 881-902.
- Bormann N, Julien PY. 1990. Scour downstream of grade-control structures. *Journal of Hydraulic Engineering* **117**(5): 579-594.
- Bridge JS. 1992. A revised model for water flow, sediment transport, bed topography and grain size sorting in natural river bends. *Water Resources Research* **28:** 999-1013.
- Chien N, Wan ZH. 1991. *Dynamics of Sediment Transport.* Academic Press of China: Beijing 563-576; (in Chinese).
- Crosato A. 1990. Simulation of meandering river processes. In *Communications on Hydraulic and Geotechnical Engineering.* Delft University of Technology: Delft, The Netherlands.
- Darby S, Delbono I. 2002. A model of equilibrium bed topography for mean bends with erodible banks. *Earth Surface Processes and Landforms* **27**(10): 1057-1085.
- Dongre N.L. 1979, Geography of Balaghat District, MadhyaPradesh Pathya Pustak Nigam Publication
- Darby SE, Thorne CR. 1996. Development and testing of riverbank-stability analysis. *Journal of Hydraulic Engineering* **122**(8): 443 -454.
- Darby SE, Alabyan AM, Van De Wiel MJ. 2002. Numerical simulation of bank erosion and channel migration in meandering rivers. *WaterResources Research* **38**(9): 1163. DOI: 10.1029/2001WR000602
- Dietrich W, Smith JD. 1983. Influence of the point bar on flow through curved channels. *Water Resources. Research* **19:** 1173-1192.
- Duan JG. 2001. Simulation of streambank erosion processes with a two-dimensional numerical model. In *Landscape Erosion and EvolutionModelling,* Harmon RS, Doe WW III (eds). Kluwer Academic/Plenum Publishers: New York; 389-427.
- Duan JG. 2004. Simulation of flow and mass dispersion in meandering channels. *Journal of Hydraulic Engineering* **130**(10): 964-976.
- Duan JG, Wang SSY, Jia Y. 2001. The application of the enhanced CCHE2D model to study the alluvial channel migration processes.*Journal of Hydraulic Research* **39**(5): 469-480.
- Engelund F. 1974. Flow and bed topography in channel bend. *Journal of Hydraulic Division* **100**(11): 1631-1648.
- Friedkin J. 1945. *A Laboratory Study of the Meandering of Alluvial Rivers.* US Waterways Experiment Station: Vicksburg. Hooke JM. 1995. River channel adjustment to meander cutoffs on the River Bollin and River Dane. *Geomorphology* **14:** 235 -253.
- Ikeda S. 1989. Sediment transport and sorting at bends. In *River Meandering,* Ikeda S, Parker G (eds).

American Society of Civil Engineers:New York; 103-115.

- Ikeda S, Parker G, Sawai K. 1981. Bend theory of river meanders, 1, Linear development. *Journal of Fluid Mechanics* **112:** 363 -377.
- Ikeda S, Nishimura T. 1986. Flow and bed profile in meandering sand-silt rivers. *Journal of Hydraulic Engineering* **112**(7): 562-579.
- Johannesson H. 1985. *Computer Simulation of Migration of Meandering Rivers.* Dissertation, University of Minnesota, St. Paul. Julien PY. 2002. *River Mechanics.* Cambridge University Press: Cambridge.
- Julien PY, Anthony DJ. 2002. Bedload motion and grain sorting in a meandering stream, *Journal of Hydraulic Research* **40**(2): 125-133.
- Kikkawa H, Ikeda S, Kitagawa A. 1976. Flow and bed topography in curved open channels. *Journal of Hydraulic Division* **102**(9): 13271342.
- Knighton AD, Nanson GC. 1993. Anastomosis and the continuum of channel pattern. *Earth Surface Processes and Landforms* **18:** 613-625.
- Lan YQ. 1990. *Dynamic Modelling of Meandering Alluvial Channels.* Dissertation, Colorado State University, Fort Collins.
- Lancaster ST, Bras RL. 2002. A simple model of river meandering and its comparison to natural channels. *Hydrological Processes* **16**(1): 126.
- Millar RG. 2000. Influence of bank vegetation on alluvial channel patterns. *Water Resources Research* **36:** 1109-1118.
- Mosselman E. 1998. Morphological modelling of rivers with erodible banks. *Hydrological Processes* **12:** 1357-1370.
- Nagata N, Hosoda T, Muramoto Y. 2000. Numerical analysis of river channel processes with bank erosion. *Journal of Hydraulic Engineering* **126**(4): 243-252.
- Nicholas AP, Smith GHS. 1999. Numerical simulation of three-dimensional flow hydraulics in a braided channel. *Hydrologic Processes* **13:**913-929.
- Odgaard A. 1989a. River meander model, I: Development. *Journal of Hydraulic Engineering* **115**(11): 1433-1450.
- Odgaard A. 1989b. River meander model, II: Application. *Journal of Hydraulic Engineering* **115**(11): 1450-1464.
- Olsen NRB. 2003. Three-dimensional CFD modelling of self-forming meandering channel. *Journal of Hydraulic Engineering* **129**(5): 366372.
- Osman MA, Thorne CR. 1988. Riverbank stability analysis. I: Theory. *Journal of Hydraulic Engineering* **114**(2): 134-150.
- Parker G. 1984. Lateral bedload transport on side slope. *Journal of Hydraulic Engineering* **110:** 197-199.
- Parker G, Andrews ED. 1986. On the time development of meander bends. *Journal of Fluid Mechanics* **162:** 139-156.
- Pizzuto JE. 1990. Numerical simulation of gravel river widening. *Water Resources Research* **26:** 1971-1980.
- Sun T, Meakin P, Jossang T, Schwarz K. 1996. A simulation model for meandering rivers. *Water Resources Research* **32:** 2937-2954.
- Sun T, Meakin P, Jossang T. 2001a. A computer model for meandering rivers with multiple bedload sediment sizes. 1. Theory. *Water Resources Research* **37**(8): 2227-2241.
- Sun T, Meakin P, Jossang T. 2001b. A computer model for meandering rivers with multiple bedload sediment sizes 2. Computer simulations.*Water Resources Research* **37**(8): 2243 -2258.
- Van Rijn LC. 1989. *Sediment transport by currents and waves.* Technical Report H461. Delft Hydraulics: Delft, The Netherlands.
- Wang SS, Hu K. 1990. Improved methodology for formulating finite element hydrodynamic models. In *Finite Elements in Fluids, Volume 8,*Chung T (ed.). Hemisphere Publishing: New York; 1127-1134.